Experimental study of room-temperature indentation viscoplastic "creep" in zirconium

S. C. Storer[1], M. E. Fitzpatrick[2,]*, S. V. Hainsworth[3], M. A. Rist[1,4]

[1]*Department of Engineering and Innovation, The Open University, Walton Hall, Milton Keynes, MK7 6AA, UK*

[2] *Centre for Manufacturing and Materials Engineering, Coventry University, Priory Street, Coventry CV1 5FB, UK*

[3] *Department of Engineering, University of Leicester, Leicester, LE1 7RH, UK*

[4]*Deceased 23 December 2011*

* Corresponding author. michael.fitzpatrick@coventry.ac.uk; Tel: +44 2477 658673

Experimental study of room-temperature indentation viscoplastic "creep" in zirconium

In this paper we have studied the mechanisms of so-called "indentation creep" in a zirconium alloy. Nanoindentation was used to obtain strain rate data as the sample was indented at room temperature, at a homologous temperature below that for which creep behaviour would be expected for this material. A high value of strain rate was obtained, consistent with previous work on indentation creep. In order to elucidate the mechanism of time-dependent deformation, a load relaxation experiment was performed by uniaxial loading of a sample of the same alloy. By allowing relaxation of the sample from a peak load in the tensile test machine, a similar stress exponent was obtained to that seen in the nanoindentation creep test. We conclude that for metals, at temperatures below that at which conventional creep will occur, nanoindentation "creep" proceeds through deformation on active slip systems that were initiated by prior loading beyond the plastic limit. It is therefore more appropriate to describe it as a viscoplastic process, and not as creep deformation.

Keywords: nanoindentation; indentation creep; viscoplasticity; zirconium alloy

1. Introduction

Instrumented indentation testing has become a popular technique for evaluating the properties of materials [1-6]. The technique has the advantages of providing continuous monitoring of force during the indentation process, which allows for calculation of material properties including elastic modulus, yield strength, and hardening exponent. In addition, the ability to use low loads and small indentations means that very local changes in hardness can be probed.

Indentation creep testing has been an area of much interest [7-15]. In a typical constant rate of loading (CRL) nanoindentation test, a dwell period is set at maximum load before unloading [7]. The maximum load is held steady for a dwell time of

typically 10 to 60 seconds to allow any time-dependent deformation mechanisms to saturate. In some materials, the indenter will continue to displace (creep) into the surface, even though there is no increase in load (figure 1). This phenomenon is usually termed “indentation creep”. Depending on the material, at the beginning of the dwell period the deformation rate can reach values of several nanometres per second, whereas by the end of a 10-20 s dwell period the value can be as low as 1 nm/s [16]. This effect occurs even at room temperature, as distinct from conventional “creep” which is generally a high-temperature (T>0.3T_m where T_m is the melting temperature in K) phenomenon in most metallic materials. Creep processes usually occur either by diffusion or by dislocation mechanisms. Keeping the dwell time short removes the “creep” effect and has the added advantage of eradicating thermal drift effects during testing [8].

Researchers [17, 18] who have investigated material creep using instrumented indentation have found that “creep” mechanisms become more active at small scales, making nanoindentation an ideal tool to investigate the relationship between strain rate and stress. High values of the stress exponent n (log strain rate / log stress) have been observed using instrumented indentation on a variety of materials [19-22]. In terms of time-dependent behaviour, under indenter loading at room temperature, materials have exhibited unusual deformation mechanisms. Ma *et al*. [22] found when testing nickel films that values of stress exponent n had significant sensitivity to their indenter loading times; however, Nogning Kamta *et al.* [23] indicate that the value of the exponent becomes constant at longer dwell times.

Previously, different values of stress exponent have been linked to the various deformation mechanisms of plasticity that, in turn, contribute to indentation creep. For example, for n values of around 1, diffusional creep may dominate, especially in

materials with a grain size < 0.4 μm. For *n* values >3, particularly in materials under high stress, it is likely that movements of dislocations in the crystal lattice are dominating the creep process [24, 25].

As yet there has been no consensus on how or why high stress exponent values occur in some materials. However, there have been suggestions that twinning may play a part [26, 27]. Deformation by twinning is known to occur in hcp materials at room temperature. Huang *et al.* [27] suggest that deformation twinning may have been operative in the deformation of Zircaloy 4 following results from relaxation tests carried out over a range of temperatures. Song and Gray [28] carried out a comparative study between twinning and slip deformation modes on pure zirconium at different temperatures. They found twinning to be the main mode controlling material deformation at very low temperatures (73 K), whereas they implicate slip as the dominating mechanism above room temperature.

Dean *et al.* [29] have indicated that the high level of scatter at long dwell times makes the method fundamentally unsuited to the determination of creep data. However, Su *et al.* [13] and Phani and Oliver [30] have shown that, either by using a material that undergoes creep at room temperature, or by testing at elevated temperature, that the results obtained from nanoindentation correlate well with those from conventional creep tests.

This paper reports an experimental study on Zircaloy 4 at room temperature, comparing results from traditional techniques of compressive nanoindentation testing and tensile load relaxation testing.

2. Experimental methods

2.2 Indentation testing

Creep is time-dependent plastic deformation of material under stress. Power-law creep behaviour, during steady state creep, is described by:

$$\dot{\varepsilon} = C\sigma^n \exp\left(\frac{-Q}{RT}\right) \qquad (1)$$

Where $\dot{\varepsilon}$ is the strain rate or creep rate, C is a constant dependent on the material, Q is the activation energy of the rate-controlling process, T is the absolute temperature, and R is the universal gas constant. n is the exponent of stress (σ).

In indentation tests, the equivalent of the stress, σ, in equation 1 is indentation hardness (H), where:

$$H = P_{max}/A_C \qquad (2)$$

P_{max} is the maximum indentation load, and A_c is the contact area of the indenter. For a Berkovich tip the contact area is approximately:

$$A_c = 24.56\ (h_c^2) \qquad (3)$$

Where $h_c = h_{max} - 0.75\ P/S$, and S is material stiffness.

The exact relationship between A_c and h_c depends on the end-tip geometry, which is typically determined by the methodology proposed by Oliver and Pharr [1].

The equation for measuring steady-state strain rate by indentation is adapted from equation 1 accordingly:

$$\dot{\varepsilon}_i = C_i\, H^n \exp\left(\frac{-Q}{RT}\right) \qquad (4)$$

where C_i is a constant (different from C in equation 1) and includes the factor relating indentation hardness to yield stress.

In materials that exhibit time-dependent behaviour when under indenter load, time-dependent deformation, often termed “creep”, occurs in the zone of plastic deformation immediately under the indenter tip, even at room temperature. Stress in the material below the indenter is at its highest magnitude nearest to the tip. This indenting stress is linked to a power law relationship representing uniaxial stress/strain behaviour, as defined in equations 1 and 4. Stress exponents range from $n = 1$ (for a Newtonian viscous solid) to $n = \infty$ (for a rigid, perfectly plastic solid) [31]. Most metals have a stress exponent value of between 1 and 10 [32-34], however, there have been experiments yielding very high stress exponents with values of 30 to 100 found using indentation testing [19-23]. This is a strong indication that the phenomenon observed is not conventional creep.

2.2 Load relaxation testing

Load relaxation is a form of uniaxial mechanical testing often used to investigate the effect of strain rate, and sometimes temperature, on the deformation of a material. The load frame of the test machine behaves elastically, whilst the test specimen behaves both elastically and plastically. The stress in the specimen is calculated from the set load and the cross sectional area of the specimen. The specimen and the load frame are treated as springs in series, and the strain rate of the specimen ($\dot{\varepsilon}_S$) can be calculated from:

$$\dot{\varepsilon}_S = \dot{\varepsilon}_E + \dot{\varepsilon} \qquad (5)$$

where $\dot{\varepsilon}_E$ is elastic strain rate, and $\dot{\varepsilon}$ is plastic strain rate.

At a pre-determined plasticity point, the crosshead motion is stopped, so in effect the actuator strain rate is equal to zero. By recording the load relaxation from this point onwards, it can be shown that the plastic strain rate in the test specimen is related to the rate of change in stress ($\dot{\sigma}$) according to the following equation:

$$\dot{\varepsilon} = -\dot{\sigma}\left(\frac{1}{E} + \frac{1}{E_{LF}}\right) \qquad (6)$$

Where E is the elastic modulus of the specimen material and E_{LF} is the elastic modulus of the load frame. For the usual case where the load frame is much stiffer than the sample being tested, it can effectively be neglected.

2.3 Indentation strain rate and stress exponents

The diameter of the deformation zone under the indenter has a linear relationship to the displacement of the indenter into the surface [35]. According to Bower *et al.* [31], even though the deformation zone under an indentation will expand during indentation loading, the related stress field in the material under the indenter does not vary to any extent. However, the indenter contact area *will* change over time. The rate at which the deformation zone boundary expands into the material is thought to be a controlling factor in the indentation creep process [32].

For a Berkovich pyramidal indenter tip, the strain rate equation is:

$$\dot{\varepsilon} = \frac{1}{h}\frac{\Delta h}{\Delta t} \qquad (7)$$

Where Δh is the change in indentation depth as a function of time Δt during the hold period. By taking the log of indentation strain rate ($\dot{\varepsilon}$) as a function of the log of indentation hardness (where $H = P/A_C$), a straight line relationship is obtained, whose

slope is the stress exponent, *n*. Figure 2 shows the output of a typical single indentation test load ramp/hold sequence performed at room temperature on Zircaloy 4 rolled plate. The data were obtained for loading of the indenter to a pre-defined peak load (10 N), then holding for 30 s at peak load. The loading time was 15 s. It was found that by the end of the hold time the strain rate had fallen to a point where the data was becoming subject to significant scatter. Nogning Kamta *et al.* [23] suggest using longer hold times of up to 1000 s, but that would not have been appropriate for our experimental configuration and resolution.

When determining the indentation strain rate ($\dot{\varepsilon}$) the following is assumed:

$$\dot{\varepsilon} = \dot{h}/h, \quad \sigma = P/Ah^2 \tag{8}$$

Where $\dot{h} = \Delta h/\Delta t$ and h is the displacement of the indent. σ is indentation hardness, P is indentation load, and A is the contact area of the indent as defined in equation 3. It is assumed that indentation hardness is proportional to stress and uniaxial strain rate is proportional to indentation strain rate [36].

The stress exponent is determined from the gradient of the peak hold data (figure 2), and defined as:

$$n = \Delta(\log \dot{\varepsilon}) / \Delta(\log \sigma) \tag{9}$$

2.4 Materials and sample preparation

Zircaloy 4 hot-rolled plate (6 mm thick) was used in this study. Samples were cross-sectioned to expose the surface in the rolling direction (RD). All coupons were wet cut using electro-discharge machining (EDM). Brass wire of 0.25 mm diameter was used for cutting. The cutting process was performed carefully at low speeds to minimize mechanical deformation. The cut coupons were then hot mounted using MetPrep

Conducto-Mount conductive mounting compound granules.

To remove surface damage caused by cutting, automated rotational grinding, at 160-170 rpm, was performed. Silicon carbide grinding papers of 500, 2500 and 4000 grit were used sequentially, whilst being constantly lubricated with water. The surfaces of specimens were washed and dried between each paper change.

Automated rotational polishing at 250 rpm was then performed prior to experimental testing of the sample. Moistened MD NAP polishing cloths were used; one each for 6, 3 and 1 µm self-lubricating diamond suspensions. Starting with the 6 µm, scant applications of the diamond suspensions were applied alternately with applications of Struers red lubricant suspension (water and oil based), whilst the cloths rotated at 250 rpm for around 20 minutes. The same process was repeated respectively for the 3 µm and 1 µm suspensions. Sample surfaces were washed and dried between each polishing sequence.

Final polishing was performed using a mixture of 50% colloidal silica suspension (OPS) mixed with 50% distilled water, applied at regular intervals to ensure the cloth is well lubricated. This OPS procedure continued until a mirror finish was achieved. Following surface preparation of the specimens, the resin mounting stubs were glued on top of aluminium stubs of the same diameter. The metal stubs provide extra stability when the material is under load of indentation.

Excellent sample preparation is the key to obtaining good Kikuchi patterns, so samples for EBSD were given an extra sequence of polishing using 0.25 µm diamond suspension. This was to reduce surface damage to a minimum before etching.

Zirconium alloys are well known for their difficulty when it comes to conventional metallography [37, 38]. Vander Voort wrote “perhaps *the* most difficult refractory metal and alloys to prepare for EBSD have been zirconium and its alloys.

Numerous approaches have been tried, using all sorts of procedures, with poor results" [38]. By preparing our Zr alloy samples using the following etchant and a newly defined four-step application process, EBSD indexing of up to 94% was achieved in this study, which was a particular success of this work.

The etchant recipe used prior to EBSD was distilled water, nitric acid, and hydrofluoric acid, mixed together in that order, in a ratio of 9:9:1.

The following four-step method of application was developed and used to etch the surface of Zircaloy 4 hot-rolled plate. The resultant surface finish led to good Kikuchi patterns.

Following grinding and polishing down to 0.25 μm suspension, the sample surface was swabbed with cotton wool soaked in etchant for three 30 s increments with less than 10 minutes in between each swabbing session. The specimen was washed and dried between each etching, prior to imaging using an optical microscope to record the extent of surface damage.

Finally after a total of 90 s swabbing, a 'puddle' of etchant was dropped onto the sample surface to cover the area. The puddle was left *in situ* for 45 s; long enough to remove all signs of surface damage.

2.5 Nanoindentation

Using a Nanoindenter XP, all specimens were indented at room temperature, in an isolated room with an ambient temperature of 21˚C. A pyramidal Berkovich diamond tip was used for all indentation tests. Tip calibration was carried out, prior to each testing session, on a reference sample of fused silica.

There are several methods of using nanoindentation to extract "creep" parameters, and these are described well by Goodall and Clyne [8]. The constant load method, first introduced by Mayo *et al*. [19], was used for this study. This method

allows for a dwell period to be set at peak indentation load and allows for ease of measurement and data analysis of the progressive strain that occurs under constant peak load.

2.6 Load relaxation test

A load relaxation test was performed on a dogbone-shaped sample of the same material. Data from the load relaxation test were analysed to find the stress exponent via stress relaxation, to be compared to the stress exponent values found under compression by indentation creep testing. Following the load relaxation test, one coupon of material was cut from the most deformed region and one from the least deformed region. Both coupons were then cross-sectioned to expose the deformation zones for analysis using EBSD. Full details are given in figure 3.

The test frame used for this experiment was an Instron 3367, with a 30 kN load cell. The acquisition software was Instron Bluehill 2. The experiment was carried out at ambient temperature. The wider ends of the dogbone specimen were used to clamp the sample onto the load frame; the clamped specimen was then aligned axially to minimise bending.

Tensile loading to 24.48 kN was applied at a constant displacement rate of the cross head of 2.5 mm per minute. Load/time data were continuously recorded to beyond the material's elastic limit, to a final stress of ~380 MPa. At this point, the loading was stopped, so that the sample strain was kept constant whilst the load decreased (relaxed) over time. Strain was measured from strain gauges affixed to both sides of the specimen. Data were acquired every 0.2 s consistently throughout the whole test period, to enable later analysis for accurate values of stress exponent *n*.

2.7 Electron back scattering diffraction (EBSD)

In order to investigate the deformation mechanisms in the Zircaloy 4 material, samples were assessed using EBSD. Two experiments were carried out. The first experiment involved looking at the deformation directly underneath the tip of a large Vickers hardness indent. For comparative analysis, a non-deformed area away from the indent was also examined using the same criteria. The second experiment involved comparing the highly deformed and non-deformed regions from coupons 'a' and 'b', as cut from the dog bone sample shown in figure 3.

The SEM used was a Zeiss Supra 55VP FEGSEM equipped with an HKL/Oxford Instruments EBSD system. Flamenco acquisition software was used to obtain the grain maps [39]. The Channel 5 suite of software programs was used to analyse the data maps from Flamenco: Tango for the grain orientation maps and Mambo for the pole figures.

3. Results

3.1 Characterization of indentation response

Initial tests were performed to three different peak loads of 0.1N, 0.5N and 10N with four different dwell periods at peak load of 5, 10, 20 & 30 s. The loading time for all tests from zero to peak load was 15 s. Ten tests were performed at each load and for each dwell period. The data from the median of those ten tests were used for analysis. Figure 4(a) shows the results from these tests, expressed as indenter displacement as a function of time at peak load. Figure 4(b) shows the nominal creep strain ($\Delta h/h_{max}$) as a function of peak load dwell time (30 s). Creep strain ($\Delta h/h_{max}$) was calculated over the

peak load dwell period for each of the three loads and is shown in figure 4b for the 30s dwell period.

In Figure 4 (a) it can be seen that the displacement vs time curves show slightly more scatter in displacement for the different dwell periods at the higher load when compared with the curves from the two lower loadings, but effectively there is virtually identical agreement between the different tests. Furthermore, in Figure 4 (b) all the curves overlay each other, irrespective of load, indicating that the strain rate is the same for each of the different loads. In an indentation test, the load is held constant over a peak load dwell period: in theory the cross sectional area should also remain constant, so stress (F/A) will remain constant. However, in the current results, because the indenter continues to displace, the contact area of the indent is increasing. Hence, the stress (F/A) is decreasing and therefore not constant.

3.2 Obtaining the stress exponent n

The stress exponent n is the slope of the graphs defined by equation 9. As seen in figure 2, there is some scatter at the start of the peak hold period, so to allow for any early extraneous drift effects to subside, the first few data points from the indentation test were not analysed. The total data set analysed included differentials from the start of the 15 s loading ramp up to the last data point of the 30 s peak hold, just before the indenter unloaded.

The results are shown in figure 5. n represents the relationship between strain rate and stress. The results show that there is a very high stress dependence of the strain rate, far higher than expected from a conventional creep process. The values of stress exponents are comparable for all four loading times, indicating that over the (limited) range of loading rates studied, there is no effect of the loading rate on the value of the

stress exponents during the subsequent indentation creep process. The mean value of n from the tests is ~40.5.

3.3 Load relaxation

Mean strain values were taken from the strain gauges as a function of time. Strain rate data were taken from the whole period of tensile stress 'relaxation', from the moment that the cross head stopped. Mean stress and strain values were calculated to generate twelve average values representing the whole relaxation period (716 s). The data were then plotted as log strain rate / log stress, to evaluate the stress exponent. The resultant graph is shown in figure 6. The value of the stress exponent for Zircaloy 4 rolled plate is obtained from the gradient of the plot as $n = 36.8$.

The load relaxation test result of $n = 36.8$ correlates well with the stress exponent values from the nanoindentation tests (figure 5), which gave a mean of 40.5. This suggests that the same deformation mechanisms are working in both the load relaxation test (tensile) and the indentation tests (compressive). What we are seeing here is not creep in the conventional sense: the results indicate that the indentation creep at room temperature, below the temperature where creep would be expected in the material studied, is related to the deformation mechanism activated during the loading process into the plastic regime, and its progression under the continuing application of a fixed load until the elastic energy stored in the sample has been relaxed below a level where the deformation rate becomes negligible. In the load relaxation test, the "creep" of the sample when the load is held is caused by the continuing motion of dislocations on slip systems activated once the yield stress of the material is exceeded, and driven by the stored elastic stress in the material. The similar load exponent obtained between the two experiments indicates that this is also what happens in indentation creep. Whilst

this meets the definition of creep as being a time-dependent deformation, the decreasing strain rate in both cases, it is strictly a viscoplastic response.

3.4. EBSD maps

Prior to the map acquisition process, a point analysis was carried out. The electron beam was positioned onto several random individual grains in the area of interest on the sample surface. This exercise provides a cross section of grain orientations or diffraction planes, in order to achieve the highest indexing percentage and therefore collect the best Kikuchi patterns.

Pre-set incremental steps of 0.5 μm were recorded over a matrix of 600 × 600 μm^2 in the region immediately below the tip of the Vickers indent. This data acquisition process was then repeated in a non-deformed region about 2 mm away, on the X-axis from, the centre line of the Vickers indent. An average indexing of around 75% was achieved during this experiment.

Figure 7a shows a CSL boundary map for the area immediately below the tip of the Vickers indent. The region of the highest deformation is arrowed. Grains showing twinning boundaries are ringed. The twins are recognised by their lenticular shape. Figure 7b shows a CSL boundary map for the non-deformed area away from the indent.

The Tango software will not produce actual twinning maps for h.c.p. materials, only cubic. So misorientation maps were produced, then angle differences across the twinning plane were measured to expose the indices. An example taken from the deformed area under the large Vickers indent is shown in figure 8. The deformed area immediately below the indent does show evidence of twinning, whereas in the non-deformed region away from the indent, no grain twinning can be seen. The twinning planes identified were predominantly in the $\{10\bar{1}2\}$ direction. This follows the findings

of others [26, 40]. However, it is unlikely that this scale of twinning is large enough to be the primary deformation mechanism.

In order to evaluate texture in the two regions around the Vickers indent, inverse pole figures were generated as shown in figure 9. No significant change in texture was seen.

3.5 Deformation in the load relaxation test

Two coupons were cut from the dogbone shaped specimen:

(1) From the central, most deformed region (coupon ‘a’ shown in figure 3)

(2) From the least deformed region in the wide section of dogbone (coupon ‘b’ in figure 3).

Each coupon was then cut again in the plane shown in figure 3. The two coupons were then mounted in conductive resin, with the cut faces (RD) exposed for analysis by EBSD. In order to obtain good EBSD indexing, the cross-sectioned surfaces were then ground, polished and etched, according to the process described earlier.

The central region of coupons ‘a’ and ‘b’ were examined by EBSD. Indexing values achieved were 87% for coupon ‘a’ and 94% for coupon ‘b’. Once again Tango software was used to produce the grain maps. Figure 10a shows a CSL boundary map of the most deformed central region of coupon ‘a’, that is, in the middle of the narrow gauge section of the dogbone specimen. Figure 10b shows a map of the least deformed end section (coupon ‘b’) cut from the wider end of the dogbone. Once again, some twin formation is seen in the deformed specimen, but at a low level.

Figure 11 shows inverse pole figures for coupons ‘a’ and ‘b’ respectively. Once again the results show twins in the most deformed specimen and no twins evident in the

non-deformed specimen. Texture between the two coupons has again not changed significantly.

Conclusions

(1) Experiments were performed to determine the origin of the indentation creep effect at room temperature, by studying a zirconium alloy by nanoindentation and load relaxation testing. The material is below the homologous temperature at which conventional creep deformation would be expected to occur. The results show that the effect seen is a viscoplastic effect rather than a true creep response.

(2) Indentation testing at four different loading rates resulted in similar values of the stress exponent *n*, indicating that in the Zircaloy 4 material there is no significant influence from loading rates on the value of the stress exponent during indentation creep.

(3) Using nanoindentation to determine the stress exponent, *n* values between 36 and 45 resulted. A uniaxial load relaxation test on the same gave a stress exponent value of $n = 36.8$, correlating very well with the results from indentation testing.

(4) A high-load Vickers indent was placed in the Zircaloy 4 and deformed and non-deformed regions were images using EBSD. Some evidence of twinning was found in the deformed region, particularly in the $10\bar{1}2$ mode, as is common in Zr alloys. However, the volume of twinning was not large enough to be determined as the predominant deformation mechanism. No evidence of twinning was found in the non-deformed sample. Sections were also taken from

deformed and non-deformed regions of the dogbone specimen used in the load relaxation test. An EBSD analysis was performed and evidence of a small volume of twinning was found in the deformed sample. Again, no evidence of twinning was found in the non-deformed sample, again confirming that twinning is unlikely to be the main deformation mechanism. The deformation is therefore driven predominantly by the viscoplastic effect.

Acknowledgements

This project was supported by the RCUK Energy Programme, and we are grateful to EPSRC for funding via the PROMINENT Nuclear Fission consortium grant. MEF is grateful for funding from the Lloyd's Register Foundation, a charitable foundation helping to protect life and property by supporting engineering-related education, public engagement and the application of research. We would also like to thank Gordon Imlach and Stan Hiller for technical support at The Open University.

Figure captions

Figure 1: Nanoindentation load:displacement trace, with a 30 s hold period

Figure 2: Indentation trace showing the initial load period (right hand portion) followed by the continuing displacement of the indenter in to the sample during the peak hold (left hand portion)

Figure 3: Dogbone samples used for load relaxation testing and EBSD

Figure 4(a): Displacement vs time plots for the Zircaloy 4 with different loads and different dwell periods. Note that the four tests at each load effectively overlap each other on the plot.

Figure 4(b): Strain as a function of time for the 30s peak load dwell period for the three different loads (taken from same data set as shown in figure 4(a)).

Figure 5: Stress exponents obtained from the indentation testing.

Figure 6: Strain rate vs stress for the load relaxation test

Figure 7: (a) EBSD map of the area underneath the large Vickers indent (twins shown ringed). The area immediately under the tip of the indent is arrowed. (b) EBSD map of a non-deformed region, 2 mm away from the large Vickers indent.

Figure 8: EBSD map showing an example of twinning in the $\{10\bar{1}2\}$ plane.

Figure 9: EBSD pole figures for (a) the deformed area immediately underneath the large Vickers indent; (b) the non-deformed region 2 mm away from the indent

Figure 10 (a): EBSD map of the most deformed area (coupon ‘a’), mid-section of the ‘relaxed’ dogbone specimen (twins shown ringed). (b) EBSD map of the least deformed area (coupon ‘b’), end-section of the ‘relaxed’ dogbone specimen.

Figure 11a: EBSD pole figure of the most deformed area (coupon ‘a’), mid-section of the ‘relaxed’ dogbone specimen.

Figure 11b: EBSD pole figure of the least deformed area (coupon ‘b’), end-section of the ‘relaxed’ dogbone specimen.

References

[1] W.C. Oliver, and G.M. Pharr, *An improved technique for determining hardness and elastic modulus using load and displacement sensing indentation experiments*, J. Mater. Res. 7 (1992), pp. 1564-1583.

[2] T.F. Page, and S.V. Hainsworth, *Using Nanoindentation Techniques for the Characterization of Coated Systems: a Critique*, Surf. Coat. Technol. 61 (1993), pp. 201-208.

[3] S.V. Hainsworth, H.W. Chandler, and T.F. Page, *Analysis of nanoindentation load-displacement loading curves*, J. Mater. Res. 11 (1996), pp. 1987-1995.

[4] S. Hainsworth, and T. Page, *Evaluation of the mechanical properties of ceramics and thin hard ceramic coatings using nanoindentation*, Nondestructive Testing and Evaluation 17 (2001), pp. 275-298.

[5] M.K. Khan, S.V. Hainsworth, M.E. Fitzpatrick, and L. Edwards, *Application of the work of indentation approach for the characterization of aluminium 2024-T351 and Al cladding by nanoindentation*, J. Mater. Sci. 44 (2009), pp. 1006-1015.

[6] M.K. Khan, S.V. Hainsworth, M.E. Fitzpatrick, and L. Edwards, *A Combined Experimental and Finite Element Approach for Determining Mechanical Properties of Aluminium Alloys by Nanoindentation*, Computational Materials Science 49 (2010), pp. 751-760.

[7] T. Chudoba, and F. Richter, *Investigation of creep behaviour under load during indentation experiments and its influence on hardness and modulus results*, Surface and Coatings Technology 148 (2001), pp. 191-198.

[8] R. Goodall, and T.W. Clyne, *A critical appraisal of the extraction of creep parameters from nanoindentation data obtained at room temperature*, Acta Mater. 52 (2006), pp. 5489-5499.

[9] K.-S. Chen, T.-C. Chen, and K.-S. Ou, *Development of semi-empirical formulation for extracting materials properties from nanoindentation*

measurements: Residual stresses, substrate effect, and creep, Thin Solid Films 516 (2008), pp. 1931-1940.
[10] I.C. Choi, B.G. Yoo, Y.J. Kim, and J.I. Jang, *Indentation creep revisited*, J. Mater. Research 27 (2012), pp. 3-11.
[11] J. Dean, A. Bradbury, G. Aldrich-Smith, and T.W. Clyne, *A Procedure for Extracting Primary and Secondary Creep Parameters from Nanoindentation Data*, Mechanics of Materials 65 (2013), pp. 124-134.
[12] M. Song, Y. Liu, X. He, H. Bei, W. Hu, F. Liu, and Z. Li, *Nanoindentation creep of ultrafine-grained Al2O3 particle reinforced copper composites*, Materials Science and Engineering: A 560 (2013), pp. 80-85.
[13] C. Su, E.G. Herbert, S. Sohn, J.A. LaManna, W.C. Oliver, and G.M. Pharr, *Measurement of power-law creep parameters by instrumented indentation methods*, Journal of the Mechanics and Physics of Solids 61 (2013), pp. 517-536.
[14] R. Machaka, T.E. Derry, and I. Sigalas, *Room temperature nanoindentation creep of hot-pressed B6O*, Materials Science and Engineering: A 607 (2014), pp. 521-524.
[15] H. Takagi, and M. Fujiwara, *Set of conversion coefficients for extracting uniaxial creep data from pseudo-steady indentation creep test results*, Materials Science and Engineering: A 602 (2014), pp. 98-104.
[16] *Advanced technical ceramics. Methods of test for ceramic coatings. Determination of hardness and Young's modulus by instrumented indentation testing*, *BS DD CEN/TS 1071-7:2003*, 2003.
[17] F. Wang, P. Huang, and K.W. Xu, *Time dependent plasticity at real nanoscale deformation*, Appl. Phys. Lett. 90 (2007), p. 161921.
[18] G. Guisbiers, and L. Buchaillot, *Size and shape effects on creep and diffusion at the nanoscale*, Nanotechnology 19 (2008), p. 435701.
[19] M.J. Mayo, R.W. Siegel, A. Narayanasamy, and W.D. Nix, *Mechanical properties of nanophase TiO_2 as determined by nanoindentation*, J. Mater. Research 5 (1990), pp. 1073-1082.
[20] J. Chen, and S.J. Bull, *The investigation of creep of electroplated Sn and Ni–Sn coating on copper at room temperature by nanoindentation*, Surface and Coatings Technology 203 (2009), pp. 1609-1617.
[21] B.N. Lucas, and W.C. Oliver, *The Elastic, Plastic, and Time Dependent Properties of thin Films as Determined by Ultra low Load Indentation*, MRS Online Proceedings Library 239 (1991), pp. doi:10.1557/PROC-239-337.
[22] Z. Ma, S. Long, Y. Pan, and Y. Zhou, *Loading rate sensitivity of nanoindentation creep in polycrystalline Ni films*, Journal of Materials Science 43 (2008), pp. 5952-5955.
[23] P. Nogning Kamta, A. Mejias, F. Roudet, G. Louis, M. Touzin, and D. Chicot, *Indentation creep analysis of T22 and T91 chromium based steels*, Materials Science and Engineering: A 652 (2016), pp. 315-324.
[24] W.B. Li, J.L. Henshall, R.M. Hooper, and K.E. Easterling, *The mechanisms of indentation creep*, Acta Metallurgica et Materialia 39 (1991), pp. 3099-3110.
[25] X.Y. Zhu, X.J. Liu, F. Zeng, and F. Pan, *Room temperature nanoindentation creep of nanoscale Ag/Fe multilayers*, Materials Letters 64 (2010), pp. 53-56.
[26] M. Preuss, J. Quinta da Fonseca, V. Allen, D.G.L. Prakash, and M.R. Daymond, *Twinning in structural materials with a hexagonal close-packed crystal structure*, J. Strain Analysis Engng Design 45 (2010), pp. 377-389.

[27] F.H. Huang, G.P. Sabol, S.G. McDonald, and L. Che-Yu, *Load relaxation studies of zircaloy-4*, Journal of Nuclear Materials 79 (1979), pp. 214-226.
[28] S.G. Song, and G.T. Gray, *Influence of temperature and strain rate on slip and twinning behavior of Zr*, Metallurgical and Materials Transactions A 26 (1995), pp. 2665-2675.
[29] J. Dean, J. Campbell, G. Aldrich-Smith, and T.W. Clyne, *A critical assessment of the "stable indenter velocity" method for obtaining the creep stress exponent from indentation data*, Acta Materialia 80 (2014), pp. 56-66.
[30] P.S. Phani, and W.C. Oliver, *A direct comparison of high temperature nanoindentation creep and uniaxial creep measurements for commercial purity aluminum*, Acta Materialia 111 (2016), pp. 31-38.
[31] A.F. Bower, N.A. Fleck, A. Needleman, and N. Ogbonna, *Indentation of a power law creeping solid*, Proceedings of the Royal Society of London. Series A: Mathematical and Physical Sciences 441 (1993), p. 97-124.
[32] B.N. Lucas, and W.C. Oliver, *Indentation power-law creep of high-purity indium*, Metallurgical and materials Transactions A 30 (1999), pp. 601-610.
[33] M.J. Mayo, and W.D. Nix, *A micro-indentation study of superplasticity in Pb, Sn, and Sn-38 wt% Pb*, Acta Metallurgica 36 (1988), pp. 2183-2192.
[34] V. Raman, and R. Berriche, *An investigation of the creep processes in tin and aluminum using a depth-sensing indentation technique*, Journal of Materials Research 7 (1992), pp. 627-638.
[35] H.M. Pollock, D. Maugis, and M. Barquins, *Characterization of submicrometre surface layers by indentation*, Microindentation Techniques in Materials Science and Engineering 889 (1986), pp. 47–71.
[36] D. Tabor, *The hardness of metals*, Oxford University Press, Oxford, 1951.
[37] M.K. Miller, X.L. Wang, D.J. Larson, and J.D. Olson, *Laser LEAP Characterization of a Zr 52.5, Cu 17.9, Ni 14.6, Al 10, Ti 5, Bulk Metallic Glass*, Microscopy and Microanalysis 13 (2007), pp. 1630-1631.
[38] G. Vander Voort, *Metallographic specimen preparation for electron backscattered diffraction*, La Metallurgia Italiana, 11-12 (2009), pp. 72-79.
[39] P.C. Paris, R.M. McMeeking, and H. Tada, *The Weight Function Method for Determining Stress Intensity Factors*, in *Cracks and Fracture, ASTM STP 601*, ASTM, 1976, pp. 471-489.
[40] E. Tenchoff, *Deformation mechanisms, texture and anisotropy in zirconium & zircaloy*, ASTM, Philadelphia, USA, 1988.

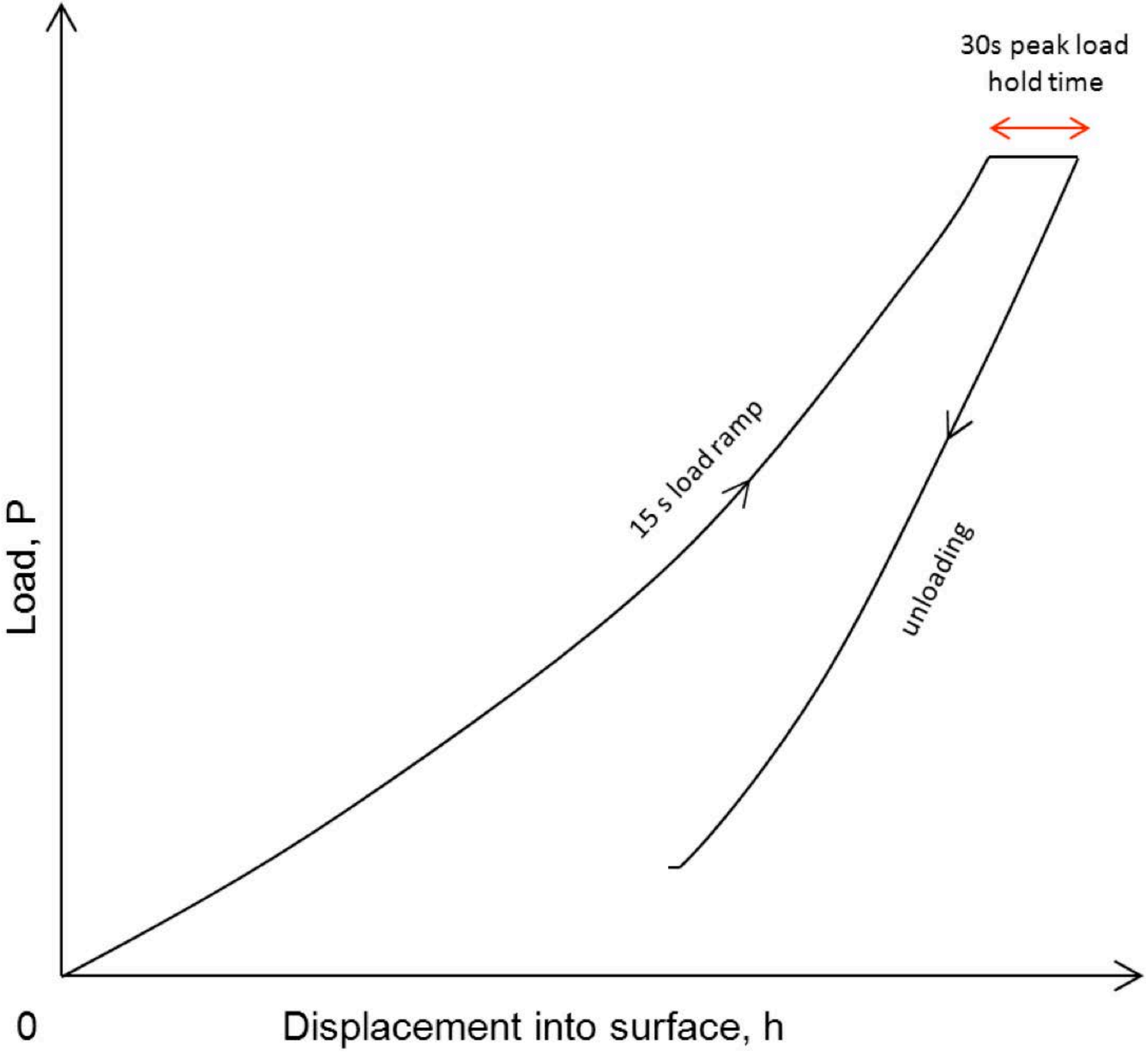
30s peak load
hold time
15 s load ramp
unloading
Load, P
0
Displacement into surface, h

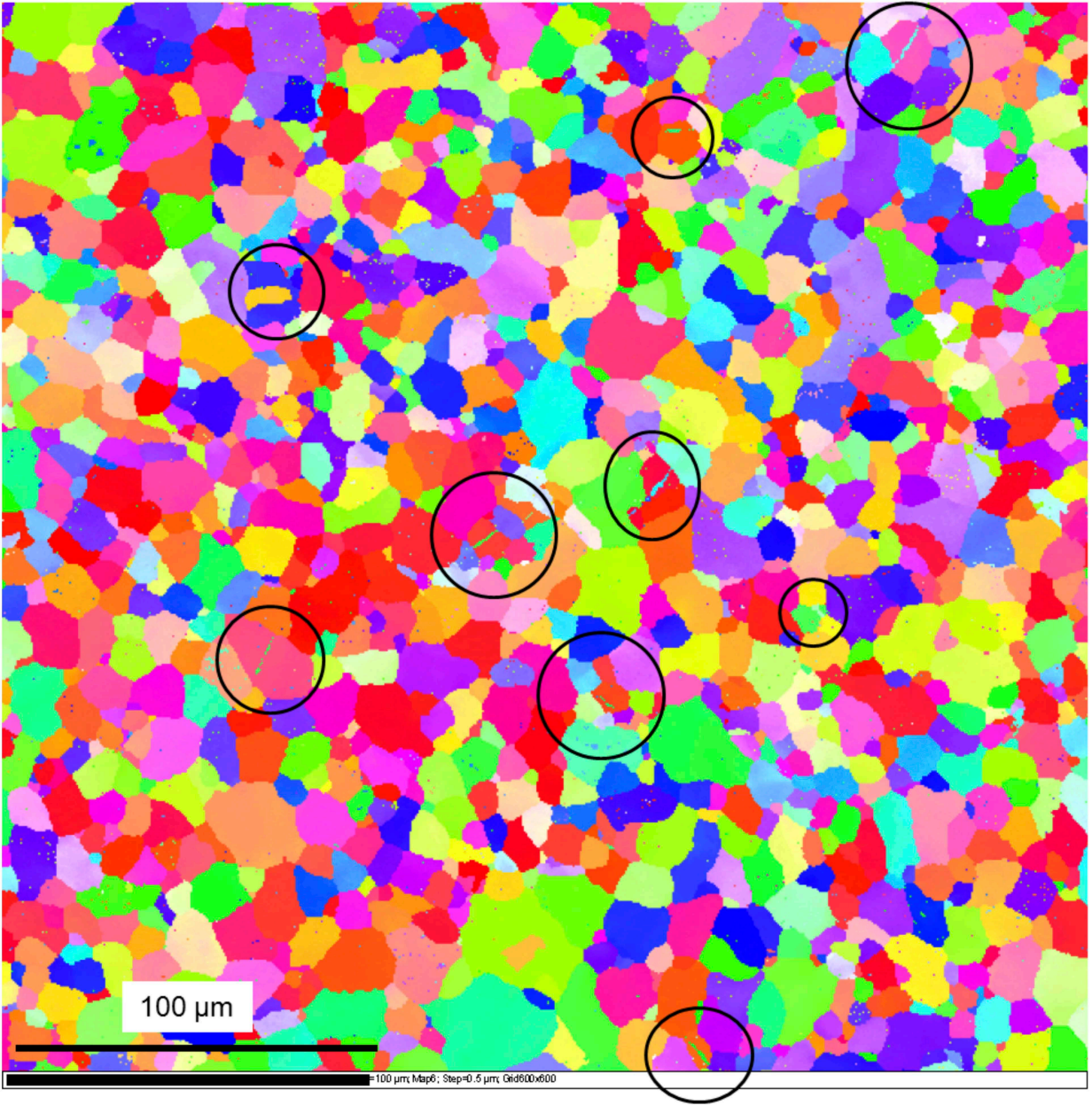
100 µm
=100 µm; Map6; Step=0.5 µm; Grid600x600

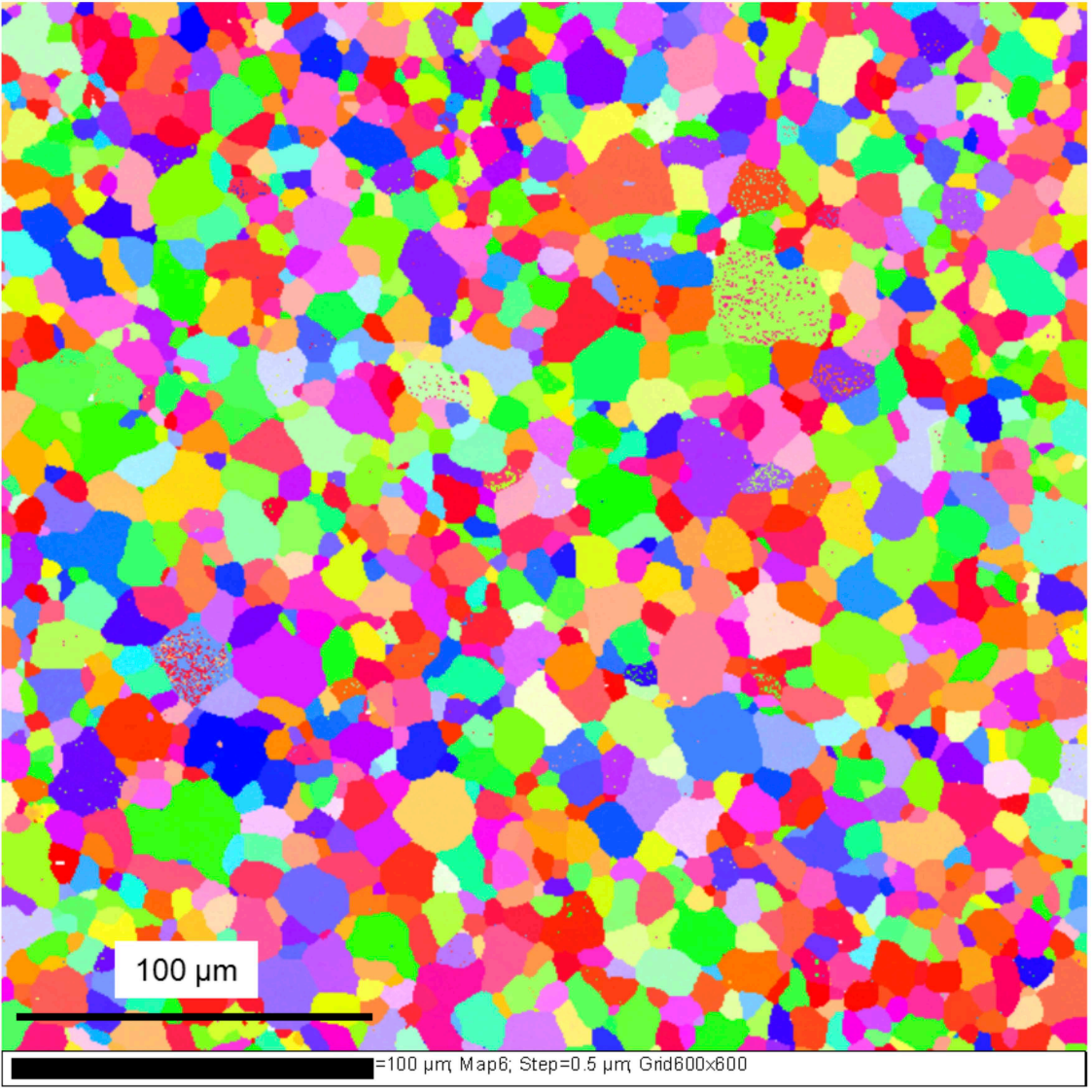
100 µm
=100 µm; Map6; Step=0.5 µm; Grid600x600

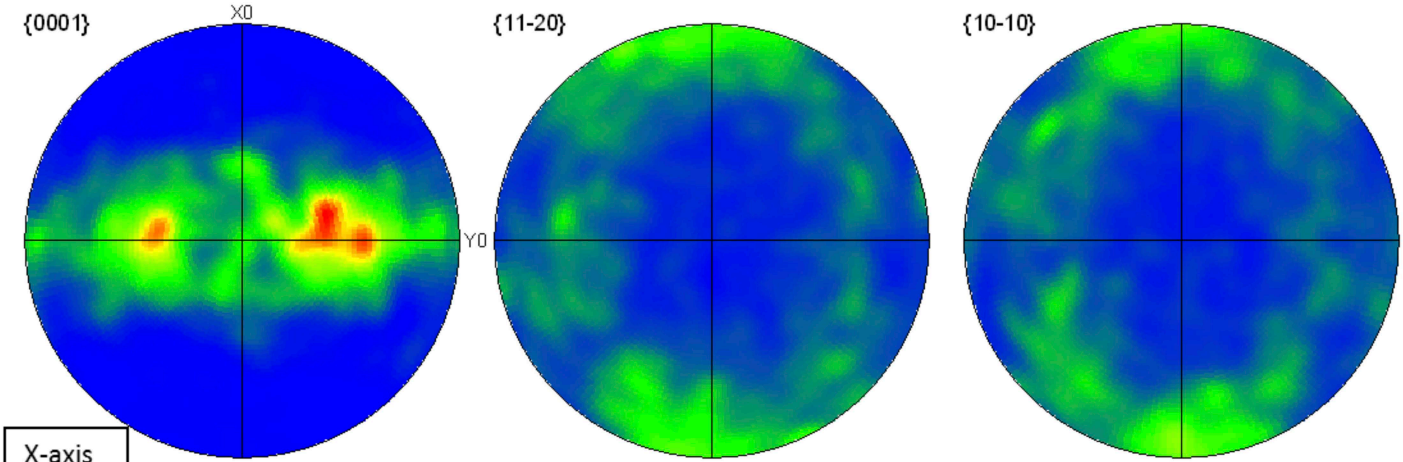
{0001}
X0
Y0
{11-20}
{10-10}
X-axis
Pole Figures
[Relax test Zry4 hot rolled
Zirc-alloy4 (6/ mmm)
Complete data set
314287 data points
Equal Area projection
Upper hemispheres
Half width: 10°
Cluster size: 5°
Exp. densities (mud):
Min= 0.00, Max= 7.07
1
2
3
4
5
6

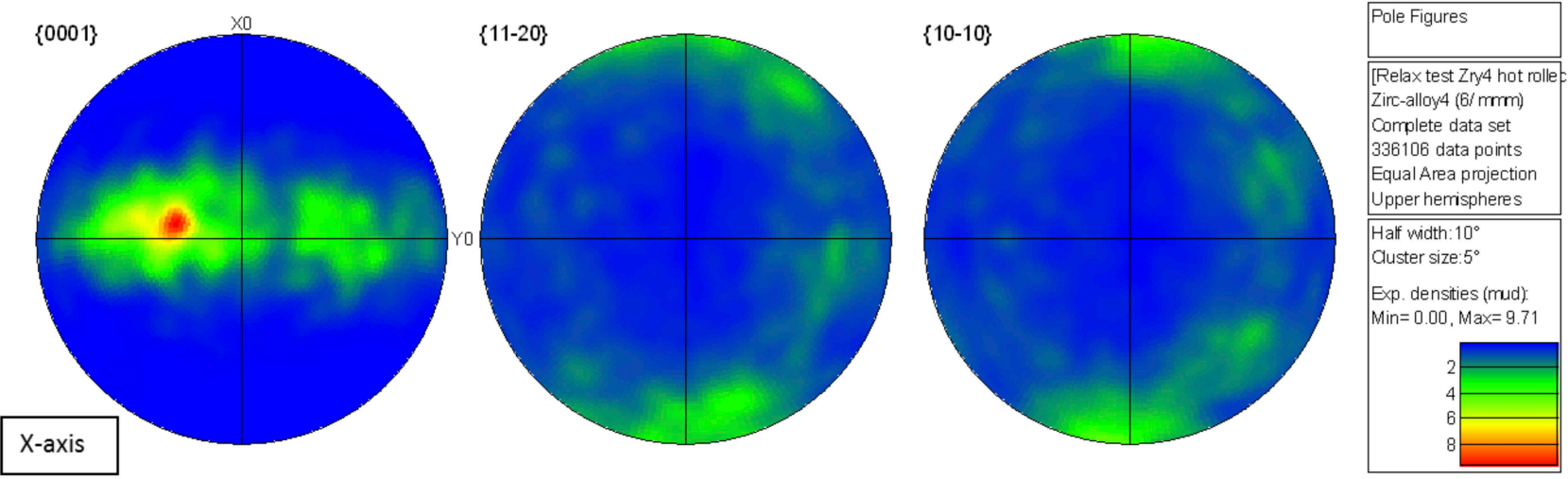
{0001}
X0
Y0
{11-20}
{10-10}
X-axis
Pole Figures
[Relax test Zry4 hot rolle
Zirc-alloy4 (6/mmm)
Complete data set
336106 data points
Equal Area projection
Upper hemispheres
Half width: 10°
Cluster size: 5°
Exp. densities (mud):
Min= 0.00, Max= 9.71
2
4
6
8

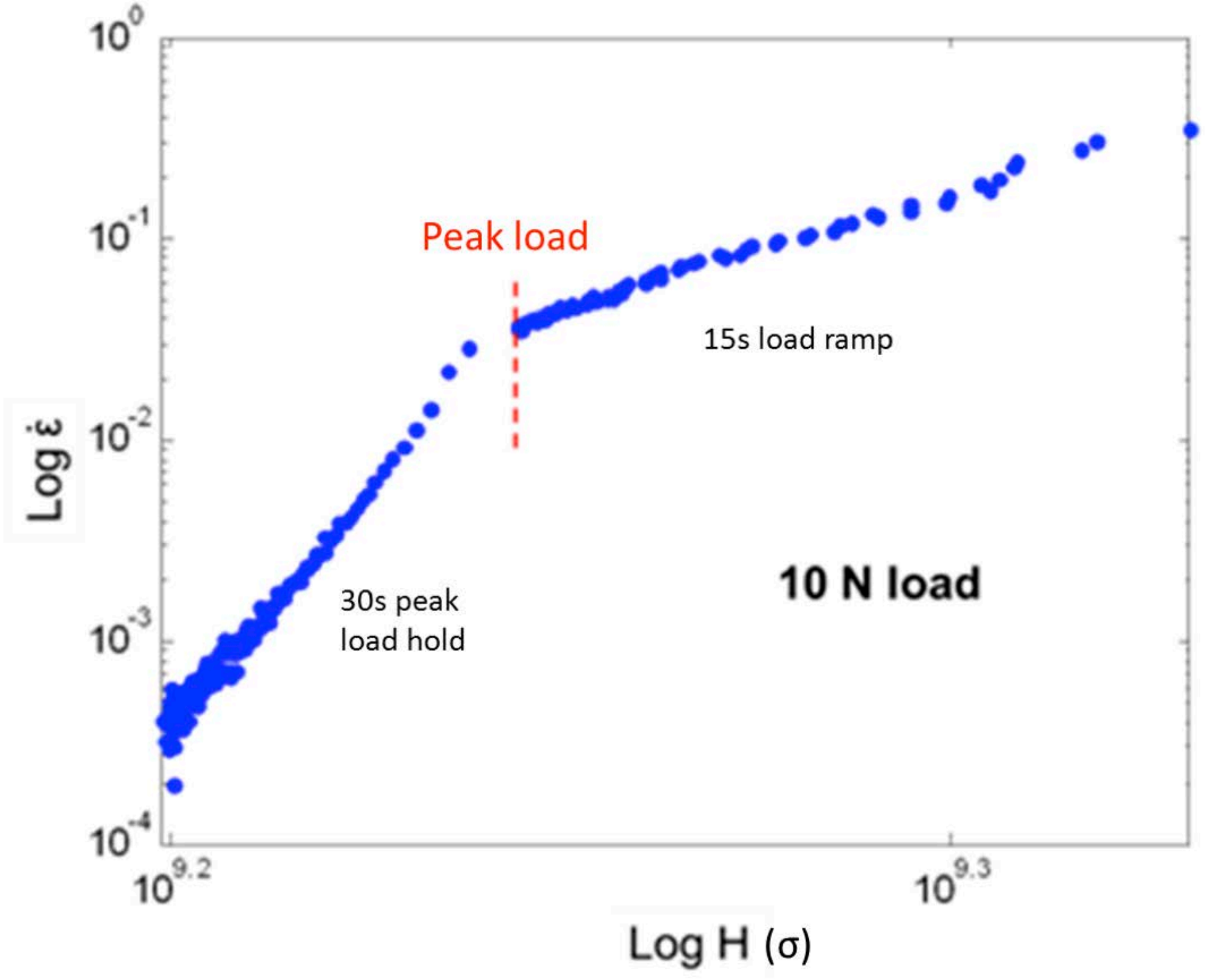
Peak load
15s load ramp
30s peak
load hold
10 N load
Log $\dot{\varepsilon}$
Log H (σ)
10^{0}
10^{-1}
10^{-2}
10^{-3}
10^{-4}
$10^{9.2}$
$10^{9.3}$

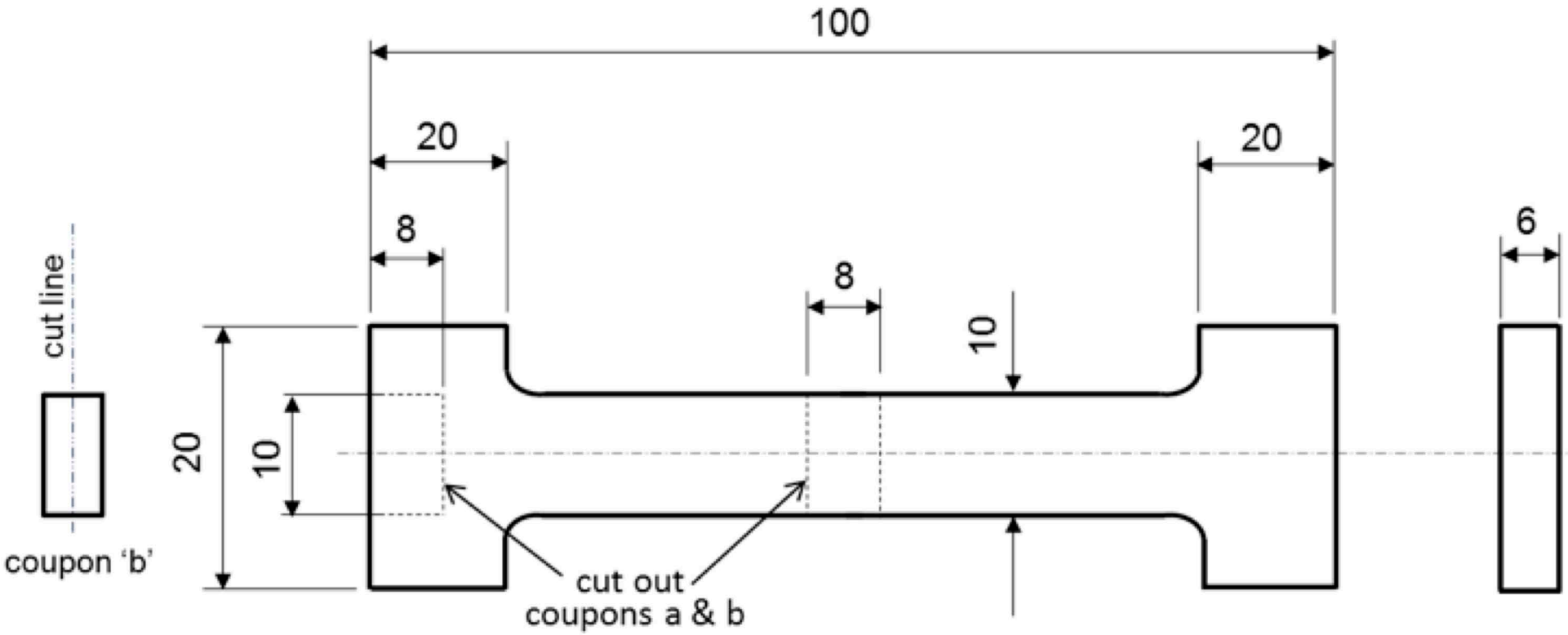

coupon 'a'

NOTES:

1. Not to scale.
2. 3rd angle projection
3. All dimensions in mm.
4. Coupons 'a' and 'b' cut through along cut line, for EBSD analysis of cut faces.

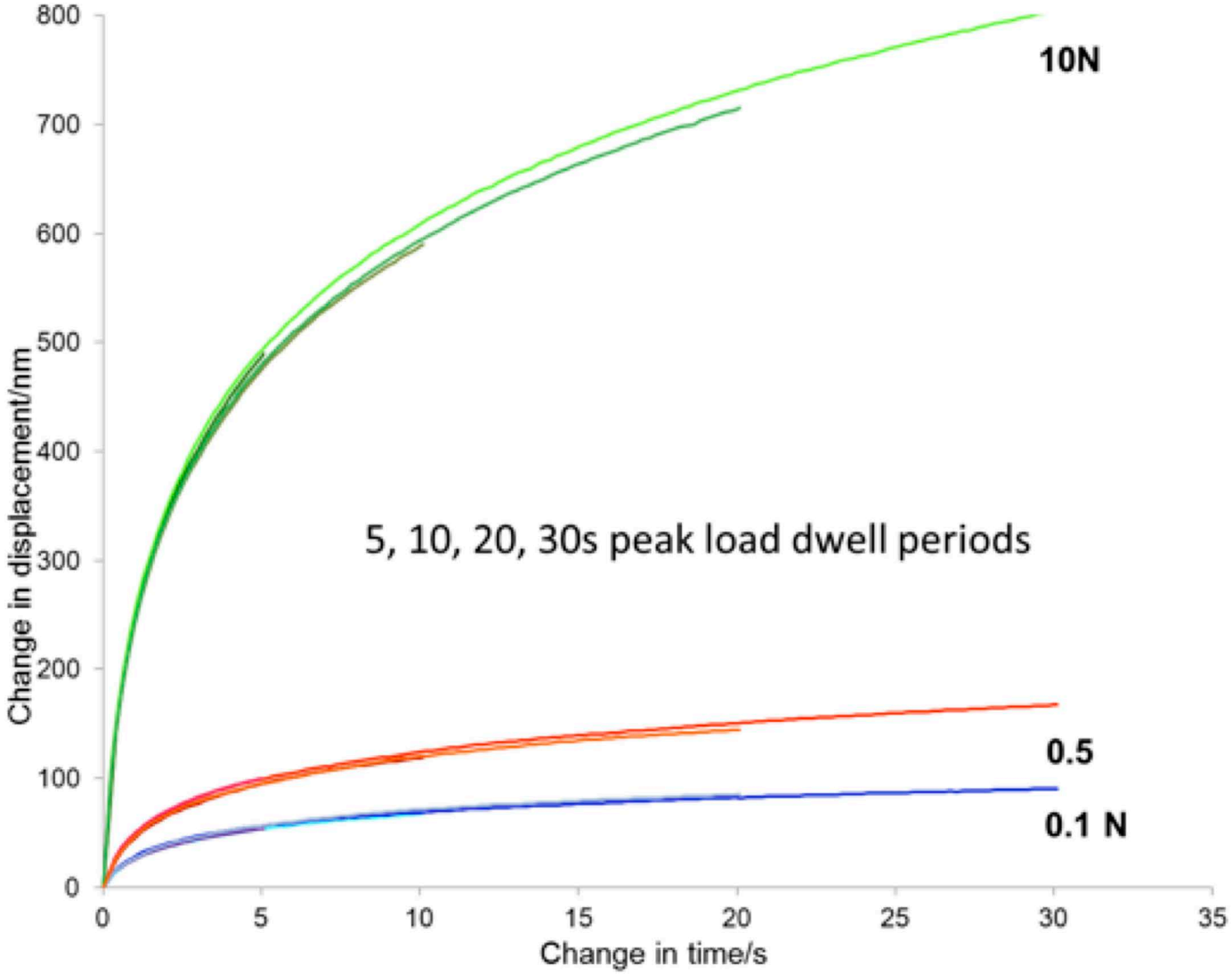
800
700
600
500
400
300
200
100
0
Change in displacement/nm
0
5
10
15
20
25
30
35
Change in time/s
10N
0.5
0.1 N
5, 10, 20, 30s peak load dwell periods

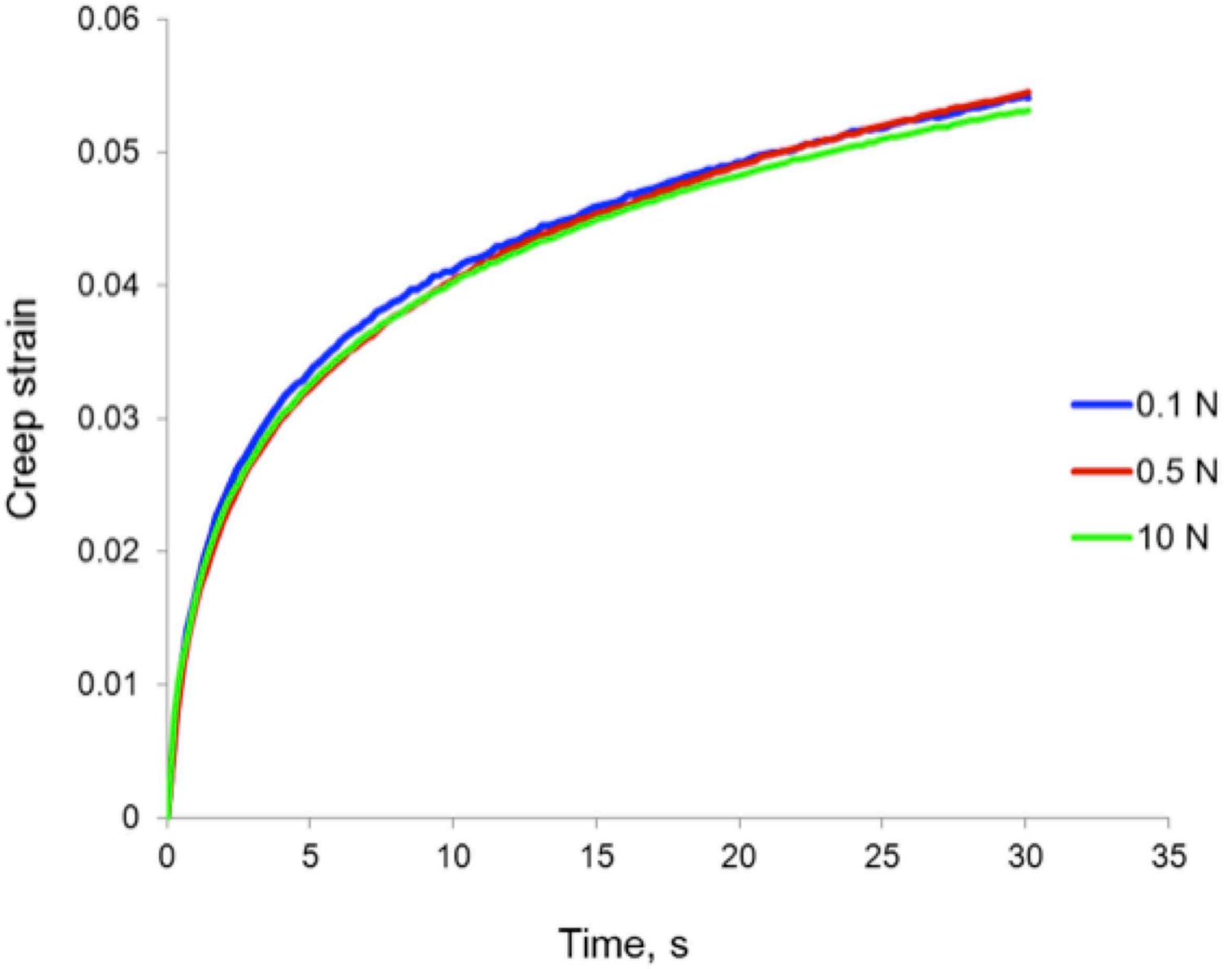
0.06
0.05
0.04
0.03
0.02
0.01
0
Creep strain
0
5
10
15
20
25
30
35
Time, s
0.1 N
0.5 N
10 N

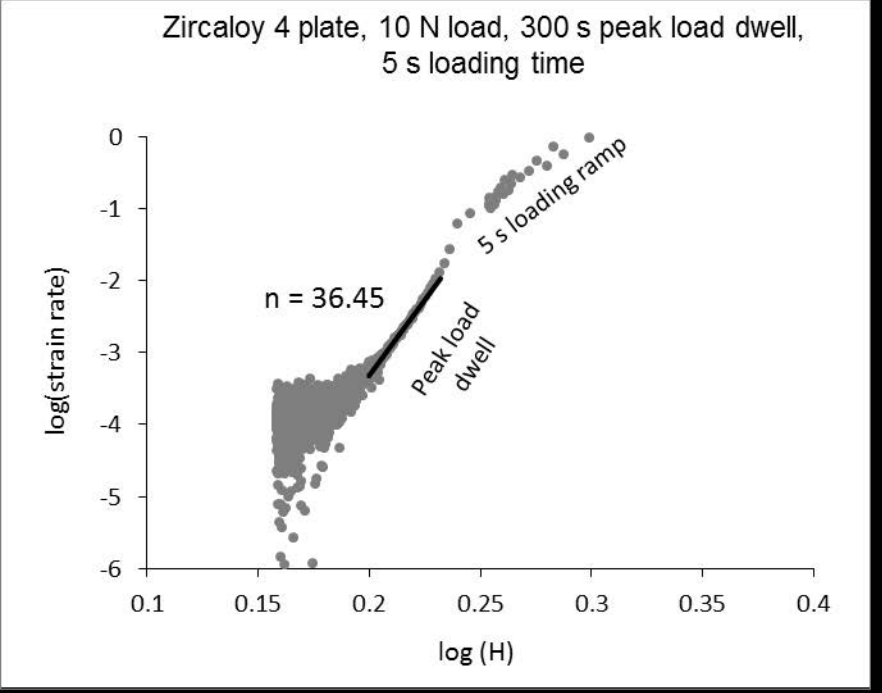
Zircaloy 4 plate, 10 N load, 300 s peak load dwell, 5 s loading time
n = 36.45
Peak load dwell
5 s loading ramp
log(strain rate)
log (H)
0
-1
-2
-3
-4
-5
-6
0.1
0.15
0.2
0.25
0.3
0.35
0.4

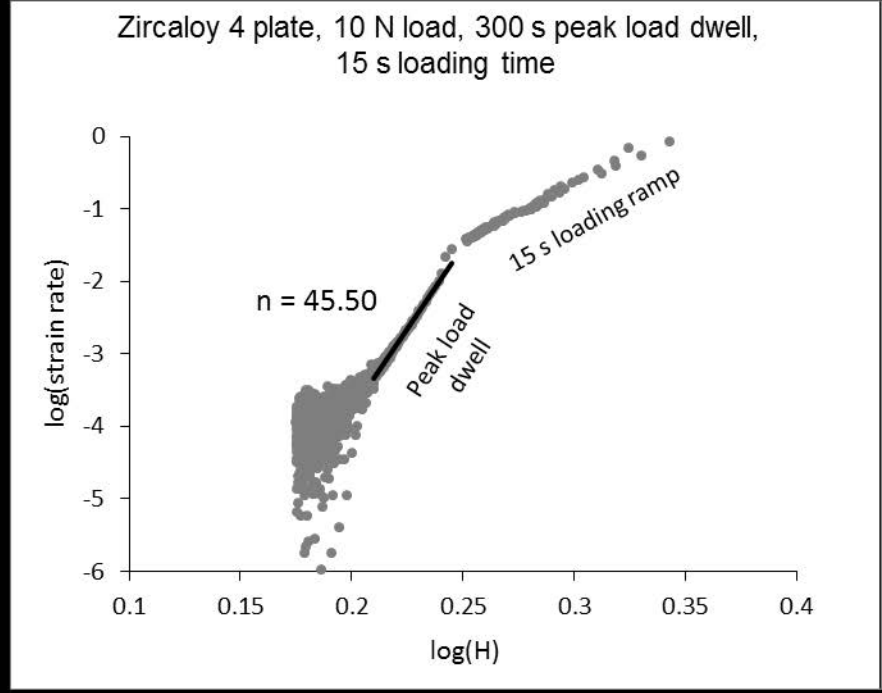
Zircaloy 4 plate, 10 N load, 300 s peak load dwell, 15 s loading time
n = 45.50
Peak load dwell
15 s loading ramp
log(strain rate)
log(H)
0
-1
-2
-3
-4
-5
-6
0.1
0.15
0.2
0.25
0.3
0.35
0.4

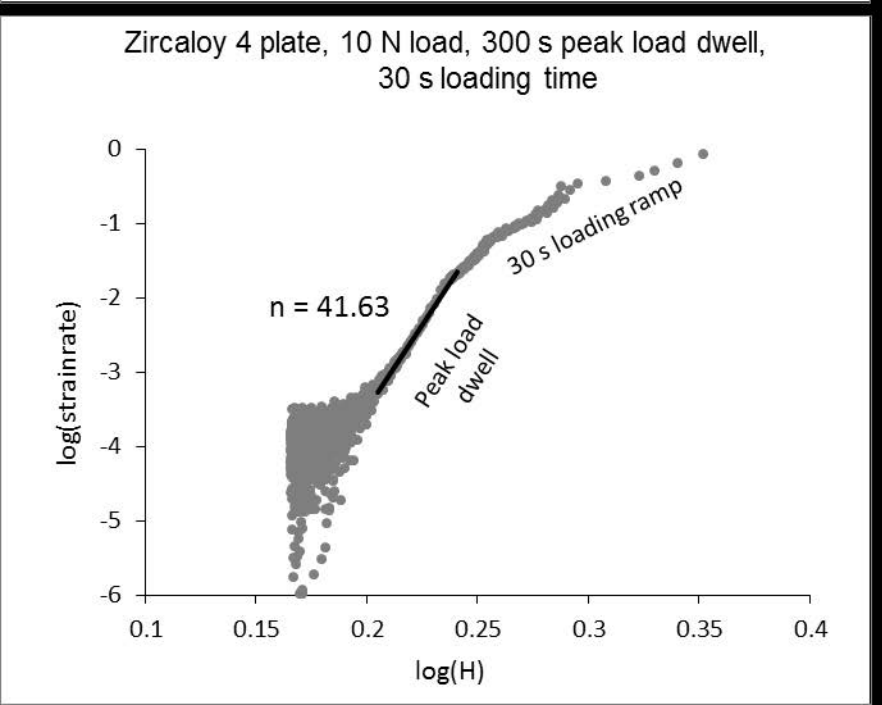
Zircaloy 4 plate, 10 N load, 300 s peak load dwell, 30 s loading time
n = 41.63
Peak load dwell
30 s loading ramp
log(strainrate)
log(H)
0
-1
-2
-3
-4
-5
-6
0.1
0.15
0.2
0.25
0.3
0.35
0.4

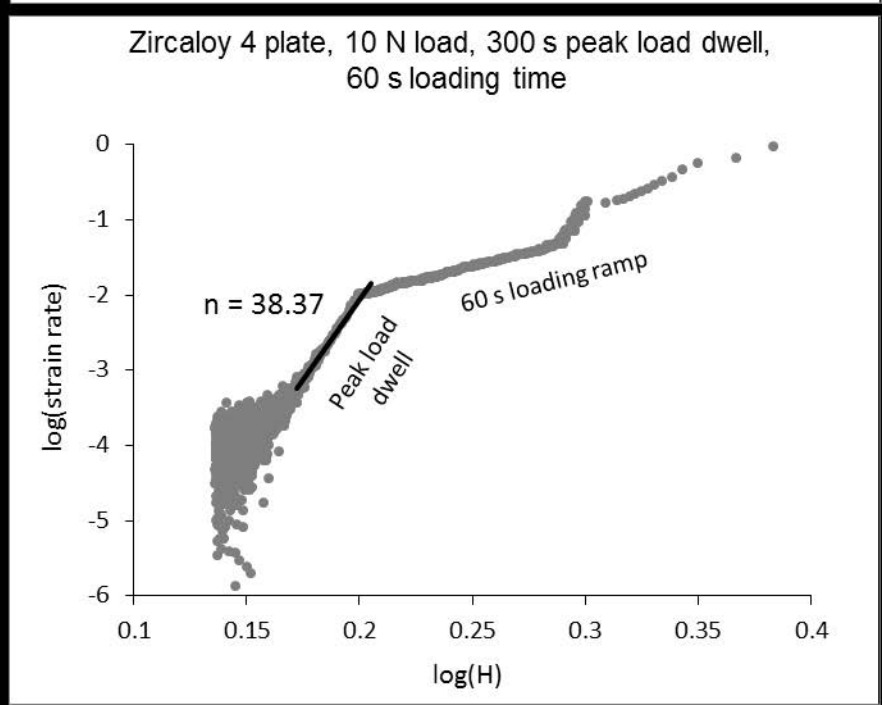
Zircaloy 4 plate, 10 N load, 300 s peak load dwell, 60 s loading time
n = 38.37
Peak load dwell
60 s loading ramp
log(strain rate)
log(H)
0
-1
-2
-3
-4
-5
-6
0.1
0.15
0.2
0.25
0.3
0.35
0.4

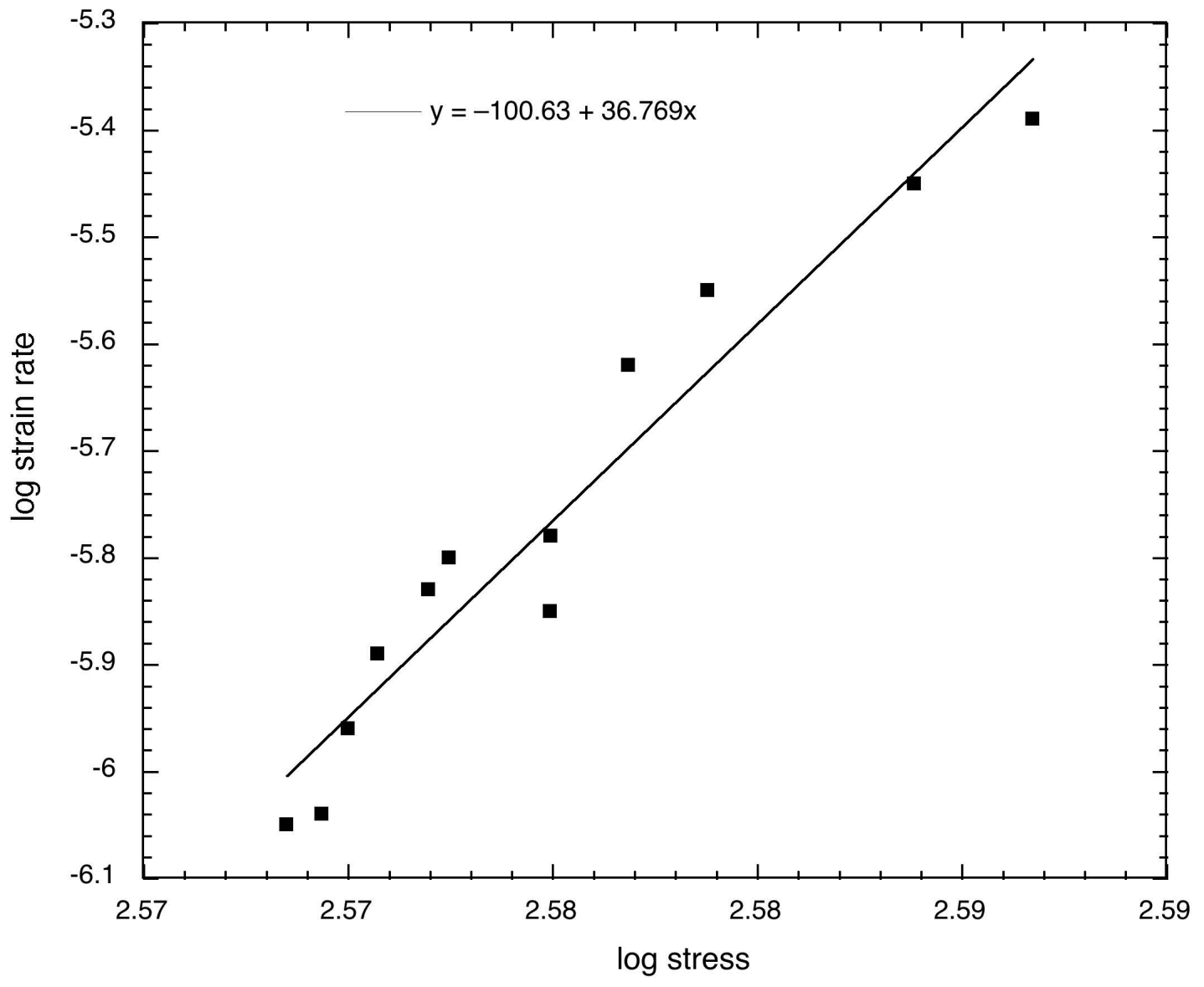
y = −100.63 + 36.769x
log strain rate
log stress
-5.3
-5.4
-5.5
-5.6
-5.7
-5.8
-5.9
-6
-6.1
2.57
2.57
2.58
2.58
2.59
2.59

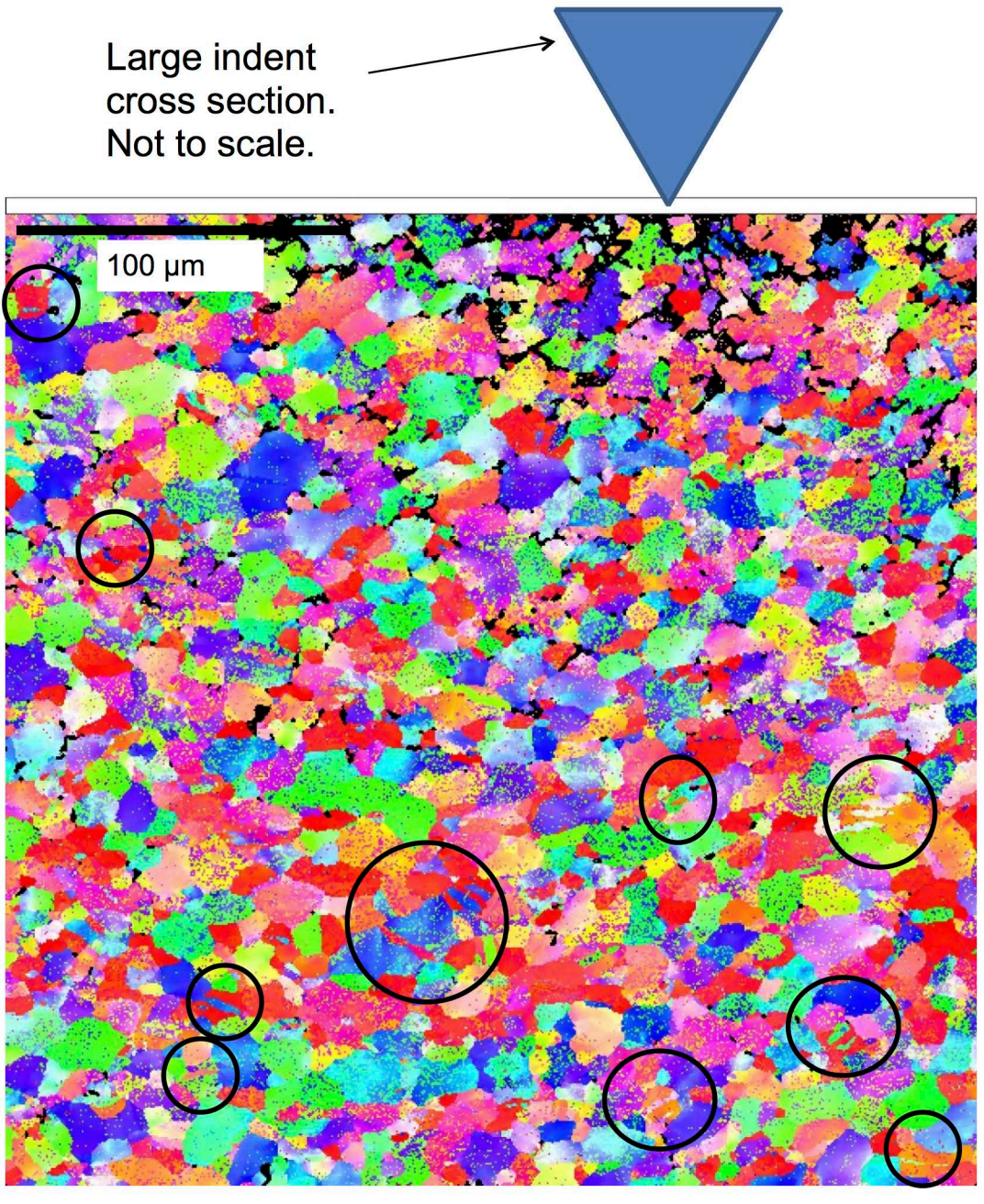
Large indent
cross section.
Not to scale.
100 µm


100 µm

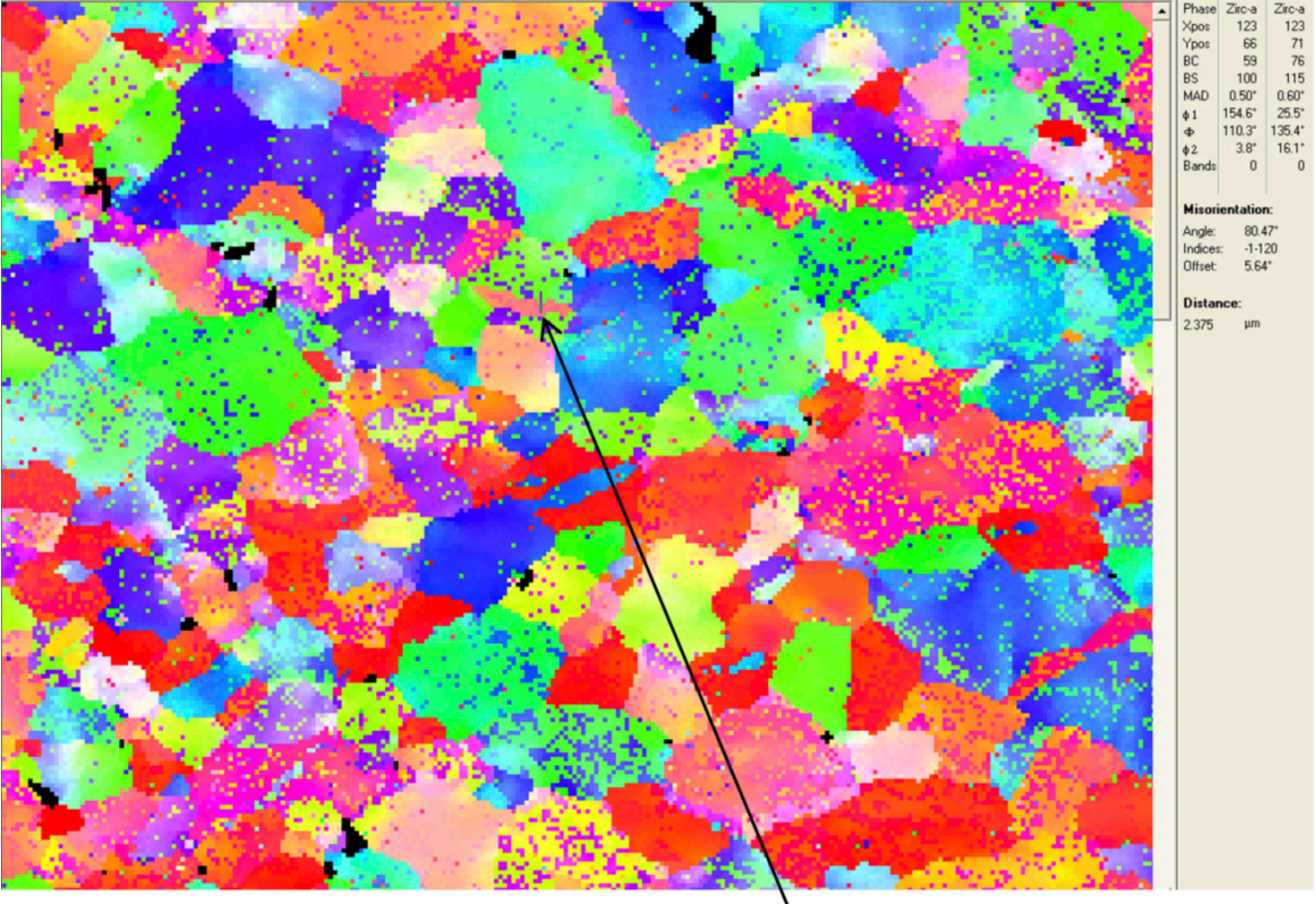
Phase Zirc-a Zirc-a
Xpos 123 123
Ypos 66 71
BC 59 76
BS 100 115
MAD 0.50° 0.60°
ϕ1 154.6° 25.5°
Φ 110.3° 135.4°
ϕ2 3.8° 16.1°
Bands 0 0
Misorientation:
Angle: 80.47°
Indices: -1-120
Offset: 5.64°
Distance:
2.375 µm
50 µm
Twinning in {10$\bar{1}$2} plane

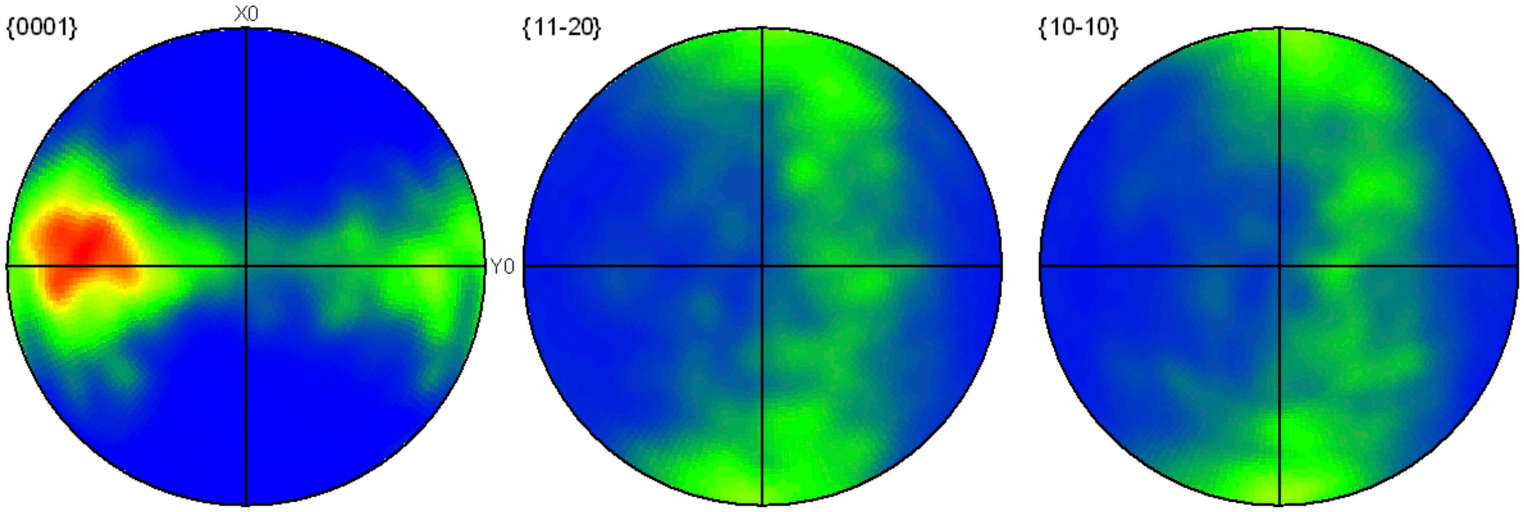

Pole Figures

[Zry4 twinning 10_03_1
Zirc-alloy4 (6/ mmm)
Complete data set
223719 data points
Equal Area projection
Upper hemispheres

Half width: 10°
Cluster size: 5°

Exp. densities (mud):
Min= 0.00, Max= 6.55

1
2
3
4
5
6

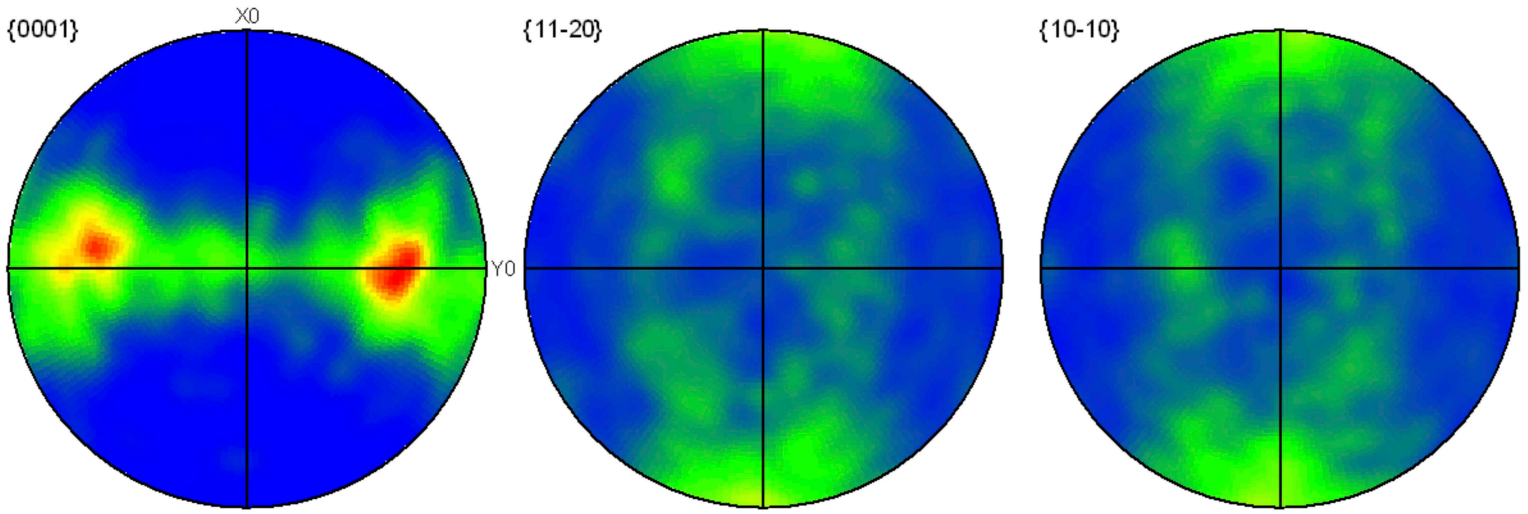
{0001}
X0
Y0
{11-20}
{10-10}
Pole Figures
[Zry4 non twinning 17_0
Zirc-alloy4 (6/ mmm)
Complete data set
334161 data points
Equal Area projection
Upper hemispheres
Half width:10°
Cluster size:5°
Exp. densities (mud):
Min= 0.00, Max= 6.46
1
2
3
4
5